Journal of Nondestructive Evaluation (2024) 43:58
https://doi.org/10.1007/s10921-024-01076-7

Characterization of Corrosion-Induced Fracture in Reinforced Concrete Beams Using Electrical Potential, Ultrasound and Low-Frequency Vibration

Tomasz Ferenc[1] · **Erwin Wojtczak**[1] · **Błażej Meronk**[1] · **Jacek Ryl**[2] · **Krzysztof Wilde**[1] · **Magdalena Rucka**[1]

Received: 3 December 2023 / Accepted: 1 April 2024

Abstract
The paper deals with the non-destructive experimental testing of the reinforced concrete beams under progressive corrosion. A series of experiments using electrical potential, ultrasound and low-frequency vibrations techniques are reported. Electrical potential and natural frequencies were used to characterise and monitor the corrosion process at its initial state. The P-wave velocity measurements were proved to be effective in quantitative assessment of the level of corrosion as it progresses. The possibility of early detection of damage using a proposed damage index and diagnostic framework is promising for possible applications in the non-invasive diagnostics of reinforced concrete elements.

Keywords Corrosion · Reinforced concrete · Non-destructive testing · Electric potential · Low-frequency vibrations · Ultrasonic waves

1 Introduction

Cement-based materials are widely used in civil and industrial structures throughout the world due to their high mechanical properties, durability, accessibility of constituents, low cost, ease of manufacture and maintenance, non-combustibility, high-temperature resistance, and low porosity [1]. As an example, concrete with reinforcement in the form of steel bars is commonly used in civil engineering structures. Despite its many advantages, such as relatively low cost, high strength, or the ability to form various shapes, it also has some disadvantages. Reinforced concrete (RC) structures are particularly susceptible to cracking, which can be caused by a number of critical factors, including environmental conditions, overloading, corrosion, dynamic phenomena, and fatigue [2, 3].

One of the main causes of damage in steel-reinforced concrete structures is the corrosion of the rebars [4]. In RC structures the steel is protected from corrosion by a thin, passive layer of hydrated iron and calcium oxides. However, due to external factors, such as the presence of carbon dioxide (CO_2) or other aggressive substances affecting the structure, e.g., chlorides from salty water, the passive layer can decompose, causing a potential difference that can be measured by, e.g., the half-cell method. This leads to local initiation of the corrosion process [5] (Fig. 1). At anodic sites, iron oxidizes and the electrons released are conducted through the steel to cathodic sites where they undergo oxygen depolarization with the formation of hydroxide ions (OH^-). Corrosion degradation of structures made of reinforced concrete is associated with a reduction in the cross-sectional

✉ Tomasz Ferenc
tomasz.ferenc@pg.edu.pl

Erwin Wojtczak
erwin.wojtczak@pg.edu.pl

Błażej Meronk
blazej.meronk1@pg.edu.pl

Jacek Ryl
jacek.ryl@pg.edu.pl

Krzysztof Wilde
krzysztof.wilde@pg.edu.pl

Magdalena Rucka
magdalena.rucka@pg.edu.pl

[1] Department of Mechanics of Materials and Structures, Faculty of Civil and Environmental Engineering, Gdańsk University of Technology, Narutowicza 11/12, 80-233 Gdańsk, Poland

[2] Institute of Nanotechnology and Materials Engineering, Faculty of Applied Physics and Mathematics, Gdańsk University of Technology, Narutowicza 11/12, 80-233 Gdańsk, Poland

Published online: 05 May 2024

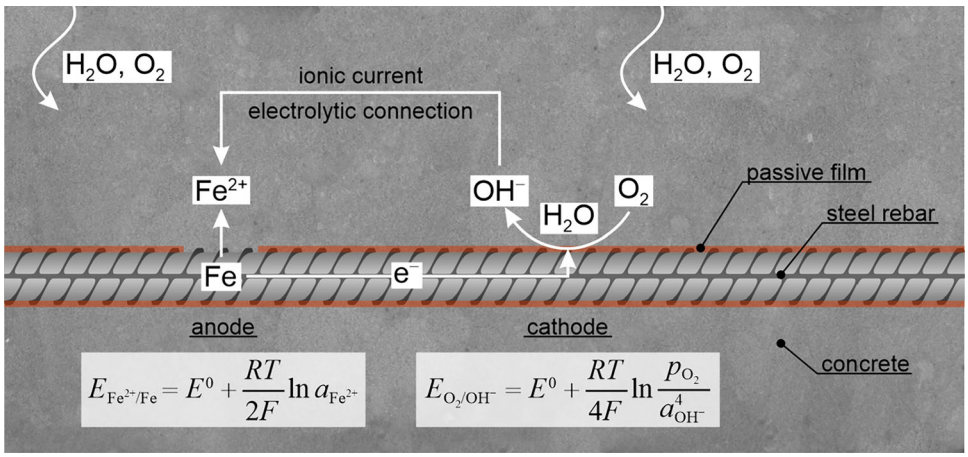

Fig. 1 Initiation of corrosion process (redrawn after [5]

area of the reinforcement, resulting in a loss of load carrying capacity of the structure, and the formation of expanded corrosion products, which lead to cracking and spalling of the concrete cover [6–8]. On the other hand, corrosion may lead to the lost of bond between the rebars and concrete [9]. Mechanical deterioration of rebars due to rusting can lead to catastrophic failure of an entire structure.

Monitoring the performance of reinforced concrete elements exposed to corrosion is becoming increasingly important to improve the safety and extend the service life of civil engineering objects [10]. The risk of failure of structures due to environmental factors is taken into account during the design process, e.g., by assuming an adequate cover of reinforcing steel rebars according to the Eurocodes standards [11] or by the appropriate selection of concrete components according to standard EN206 which indicates, e.g., minimum cement content or limits of mineral additions for specific exposure classes. However, corrosion diagnostics are not required during operation. As a result, there is no systematic method to verify whether or not corrosion is present in a structure. A crucial problem is that rebars are embedded in concrete and it is not possible to visually assess their actual condition, so the corrosion process can occur without significant external symptoms. It is therefore beneficial for the safety of structures to use integrated non-destructive diagnostic techniques to detect and quantitatively assess corrosion at different stages [5, 12]. Recently, in addition to destructive methods, which require the reinforcement to be exposed and inspected for the presence of corrosion, there have been non-destructive methods that can be used to detect corrosion. By inducing low-frequency vibrations, it is possible to determine the natural frequencies and mode shapes of the structure and to examine their variation due to the corrosion process [13–15]. Other approaches that are effective in detecting corrosion include non-invasive techniques based on guided wave propagation and ultrasonic scanning [16–22], acoustic emission [23–25], X-ray computed tomography [26–28], fibre Bragg grating [29] and ground penetrating radar [30].

Despite many successful applications of non-destructive techniques in corrosion diagnostics, the development of new approaches effective in monitoring the corrosion of reinforced concrete structures is of great importance in civil engineering. The main contribution of the current paper is a study on the integrated application of different diagnostic methods for monitoring corrosion in reinforced concrete beams. The proposed approach indicates whether corrosion is present and how its effects may affect the beams. Extensive investigations using potential measurement, low-frequency vibration, and ultrasonic wave propagation have been carried out on three beams subjected to accelerated electrochemical corrosion. The novel element of the research is the development of a two-stage diagnostic framework for the characterisation of corrosion-induced concrete fracture in reinforced concrete elements. A damage index based on the variation of the P-wave velocity has been proposed to indicate the onset of corrosion-induced fracture.

2 Description of Specimens

2.1 Materials

Three reinforced concrete beams, designated B1-B3, were analysed in the paper. All three specimens were prepared in a single manufacturing process using water, cement, aggregate, and admixture with a ratio W/C equal 0.5. The Portland cement type CEM I 42.5 R was used. Both fine aggregate in the form of natural washed sand with grain size is 0–2 mm and a density 2650 kg/m^3 and the coarse aggregate in the form of natural pebbles with grain size 2–8 mm and 8–16 mm and density 2650 kg/m^3 were used. Moreover, the superplasticizer was added to increase homogeneity and workability.

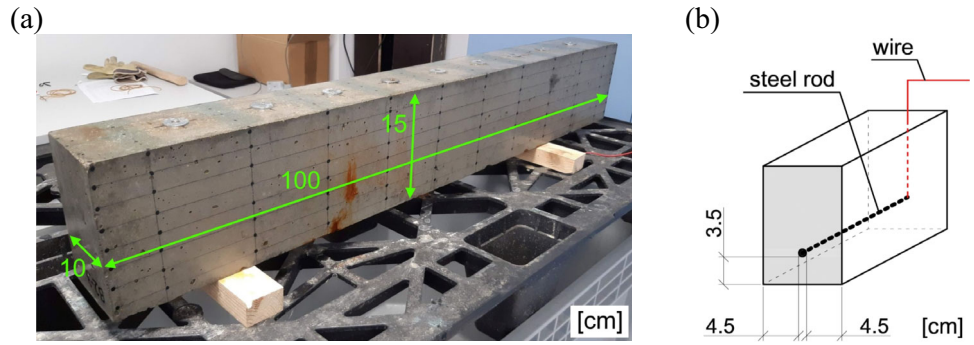

Fig. 2 Beam specimen: **a** overall view, **b** cross section

The exact recipe of concrete is as follows: cement CEM I 42.5 R—330 kg/m^3, water—165 kg/m^3, aggregate 0–2 mm (sand)—710 kg/m^3, aggregate (gravel) 2–8 mm—664 kg/m^3, aggregate (gravel) 8–16 mm—500 kg/m^3 and superplasticizer—2.31 kg/m^3. All components were mixed in a mechanical mixer. The consistency of the mixture was S3 (according to the slump test). Compressive strength was determined after 28 days on cubic samples with dimensions 10 × 10 × 10 cm and amounted 43.63 MPa which corresponds to 39.27 MPa as for cubic samples 15 × 15 × 15 cm.

As a reinforcement, a single steel bar with a diameter φ10 mm and a length 93 cm was used. The steel class is B500SP with a yield point equal to $f_{yk} = 500$ MPa. Its chemical composition is as follows: C—0.25%, Mn—1.65%, Si—0.60%, P—0.055%; S—0.055%, Cu—0.85% and N—0.013%, with a carbon equivalent (C_{eq}) not exceeding $C_{eq,\max} = 0.52\%$.

2.2 Specimens

Three specimens designated as B1-B3 were prepared with dimensions of 10 × 15 × 100 cm^3 (Fig. 2a). All of them were subjected to progressive corrosion. Three beams with identical geometrical and material parameters were tested to compare the results obtained from the three corrosion processes and to check that the results obtained are not random. The single reinforcing bar was embedded in the centre of the cross-sectional width and at a distance (bar cover) of 35 mm from the bottom face (Fig. 2b).

To initiate the corrosion process in the specimens, a 1 mm wire was connected to the end of the steel bar by soldering using a fusible metal alloy. To improve the bond, the steel bar was heated to a high temperature by a gun heater. The joint was then secured with heat shrink tubing.

3 Description of Methods

The experimental program involved measuring the properties of the specimens as the corrosion of the beams progressed. Electrical potential, low-frequency vibrations, and ultrasonic waves were used to assess the effect of corrosion on beam properties, such as corrosion potential value, free frequencies, mode shapes with damping ratios, and time of waves penetrating specimens, respectively. All the experiments were carried out in the laboratory at a room temperature of about 20ºC.

3.1 Accelerated Electrochemical Corrosion

The corrosion process was artificially induced to carry out experimental laboratory tests to quickly assess the condition of the samples.

To initiate and accelerate electrochemical corrosion, specimens can be immersed and maintained in a corrosive electrolyte, such as sodium chloride (NaCl) solution. The NaCl content in the solution may vary but usually is about 3–3.5% [19–21, 31, 32]. A constant current is then passed through the reinforcement in the sample, which is treated as the anode. To complete the current flow, another rod, acting as an auxiliary electrode (cathode), is also immersed in the solution. A current density will be imposed through the reinforced bar, which corresponds usually to a value of about 0.2–0.3 mA/cm^2 (milliampere per square centimeter) [13, 14, 16, 32, 33].

To initiate electrochemical corrosion, the specimens were immersed in the tank containing 3.5% sodium chloride (NaCl) solution (Fig. 3). The reinforced bars were connected to the laboratory power supply through the wires, as well as the additional steel rod (auxiliary electrode, cathode) placed in the tank. A constant current flow was generated by a power supply. A current density of 90 mA, equivalent to 0.3 mA/cm^2, was imposed through the reinforcing bar.

The experimental program consisted of twenty-four measurements. Each measurement was carried out after a predetermined number of days of keeping the specimens in sodium chloride solution with breaks for drying and experiments. First, the specimens were tested before the corrosion process started (D0). Measurements were then taken (D1) after the specimens had been kept in the NaCl solution for one day and

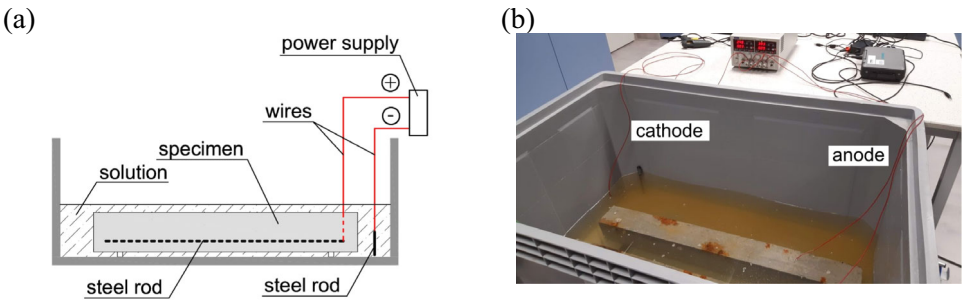

Fig. 3 Experimental setup of accelerated electrochemical corrosion: **a** scheme, **b** overall view with power supply and specimens

dried for approximately 18 to 20 h. After that, the specimens were re-immersed and kept in the solution for the next number of days until they dried, and the next measurement was performed. The number of days the specimens were kept in the solution is summarised in Table 1 and was adopted based on e.g. [19–21, 31, 32]. The measurement schedule was designed so that shorter measurement intervals occurred at the beginning of the tests when cracks were expected to occur. In turn, longer intervals were adopted in the subsequent measurements. The table does not include the drying time and the experiments.

3.2 Corrosion Potential Measurement

The method for corrosion potential measurement is standardised and described in ASTM C876-15. The method is based on the measurement of the potential difference that occurs between the steel rod in the concrete and a reference electrode placed on the concrete surface. The experiment was performed using the Proceq Profometer Corrosion equipment which is a high-impedance voltmeter (Fig. 4). The copper—copper(II) sulfate (Cu|$CuSO_4$) ($E^0 = 0.314$ V vs SHE) was used as a reference electrode. Typical values of magnitude for the half-cell potential of steel bars in concrete measured against the reference electrode can be in the range from –1000 mV to + 200 mV (vs Cu|$CuSO_4$). In general, the lower (more negative) the potential measured, the greater the likelihood of corrosion. However, the ASTM C876-15 standard gives the threshold values of the potential: if it is − 350 mV vs Cu|$CuSO_4$ or lower, there is a 90% probability that corrosion will occur, if it is − 200 mV vs Cu|$CuSO_4$ or higher, there is a 90% probability that corrosion will not occur, and between these values the measurement is uncertain.

The electrical potential was measured by placing the reference electrode on the bottom surface of the beams, in ten points along the length with the constant distance of 10 cm between, and three points across the width, giving 30 measured points. However, the values from the width were averaged, resulting in 10 points (e1–e10) across the specimen length.

3.3 Low-Frequency Vibrations

To measure low-frequency vibrations, the beams were mounted on steel supports with a distance of 95 cm between them. Thus, specimens were set free on both sides for a length of 2.5 cm. Additionally, rubber bearings were inserted between specimens and support to isolate beam vibrations from the test stand. Free vibrations were induced by means of a modal hammer PCB Piezotronics Inc. The impulse force $p_k(t)$ was applied in nine points (p1-p9) presented in Fig. 5. The structural response $a_i(t)$ was measured simultaneously utilizing accelerometers located in nine points (a1-a9) on the bottom surface of the beams, directly below points p_k, which were located ath the upper surface of the beam. The distance between the points (p_k and a_i) was therefore 10 cm in each measurement. Time dependence on acceleration was measured in a vertical direction only. To collect measurement data, the Siemens PLM Software LMS SCADAS system acquisition system was used.

The measured signals, both input and output, were loaded to the MATLAB environment and then, by means of self-written algorithms, transformed according to Fast Fourier Transform (FFT) and then the Frequency Response Functions (FRFs) were calculated from the formula (1):

$$H_{ik}(\omega) = \frac{a_i(\omega)}{p_k(\omega)}, \tag{1}$$

where $H_{ik}(\omega) = \mathbf{H}(\omega)$ is FRF function in the form of a matrix with i rows and k columns, while $a_i(\omega)$ and $p_k(\omega)$ are output and input signals transformed according to FFT, respectively. The absolute value of the chosen element of the FRF is presented in Fig. 6a. Both, natural frequencies and damping ratios can be determined from the function peaks. The value of frequency is directly read from abscissae where the peak occurs. To smooth the frequency response functions, especially in a higher range of frequencies, and thus improve the accuracy of calculations, the functions were approximated according to the Gauss function.

To determine made shapes of the beams, imaginary parts of FRFs were computed. For the calculations, a single row (or column) can be chosen. However, to avoid points, where

Table 1 Measurement designation and the corresponding number of days that specimens spend in solution

Measurement label	D0	D1	D2	D4	D5	D6	D8	D9	D10	D12	D13	D14	D17	D19	D22	D28	D34	D40	D46	D52	D58	D64	D70	D76
Specimens immersion days	0	1	2	4	5	6	8	9	10	12	13	14	17	19	22	28	34	40	46	52	58	64	70	76

displacement for a specific mode shape is near zero, e.g. mid-length point for a second mode shape, a specific row must be taken into account. Thus, to present the second mode shape (Fig. 6b) the third row was picked. Then, the amplitudes corresponding to the second frequency were identified and drawn on the diagram taking into account their values and the location of the point along the specimen length. The obtained line presents the mode shape. Analogous algorithms can be used to obtain the first or the third mode shape.

3.4 Ultrasonic Waves

Another experiment consisted of the excitation and measurement of ultrasonic waves using ultrasonic transducers at several points on the surface of tested specimens. In this study, a wave characteristic in the form of time of flight through the beam cross-section was used to detect and evaluate the degree of corrosion. The tests were performed with the use of an ultrasonic pulse velocity analyzer (UPV) Proceq Pundit PL-200. The device was equipped with exponential P-wave transducers with a carrier frequency of 54 kHz. According to the manufacturer's recommendations, the transducers can be used when the maximum grain size is 34 mm and the minimum dimension of the tested sample is 69 mm (both requirements are satisfied in the current study). The transducers do not require the use of a gel couplant, providing fast and robust measurements.

The propagating P-wave signals can be collected in a selected number of paths for all measurements. During the tests, 156 signals were collected at points numbered 1–156 (Fig. 7), running from side to side of each beam (paths 1–96) and from top to bottom (paths 97–156). One of the transducers acted as an exciter whereas the second one was a sensor. The collected signals were further processed to determine the time of flight (TOF) of the wave. As a result, the P-wave velocity was determined for each path based on the TOF and the lengths of wave propagation paths.

A self-written algorithm was used to determine the time of flight. To eliminate noise, all signals were additionally filtered using a sixth-order low-pass Butterworth filter with a cutoff frequency equal to 120 kHz.

4 Results

4.1 General observations

During each measurement D0-D76, general observations were made in addition to the experimental methods described above. First of all, after removing the specimens from the solution they were carefully inspected for cracks occurrence. During the first measurements (D0–D6), no changes were observed on the surface of the specimen. However, during

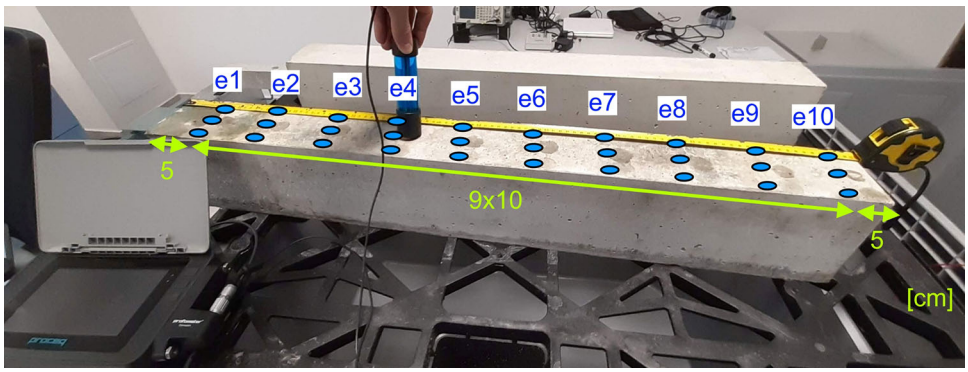

Fig. 4 Experiment setup for corrosion potential measurement: **a** overall view, **b** point electrode with copper sulphate half-cell

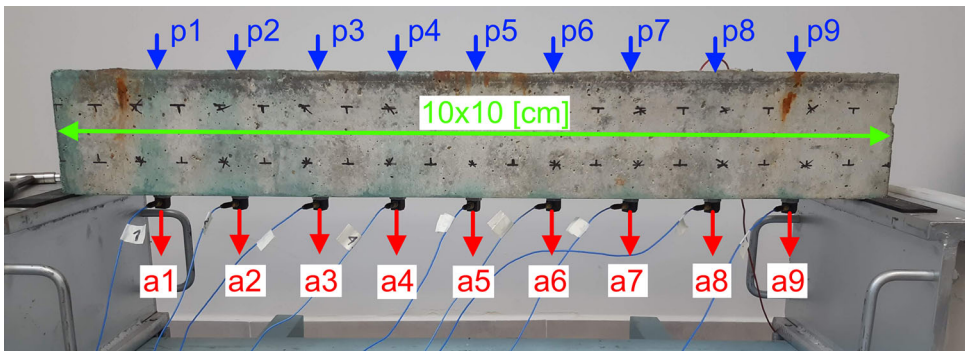

Fig. 5 Location of accelerometers (a1–a9) and applied impulse forces (p1–p9) for low-frequency vibrations

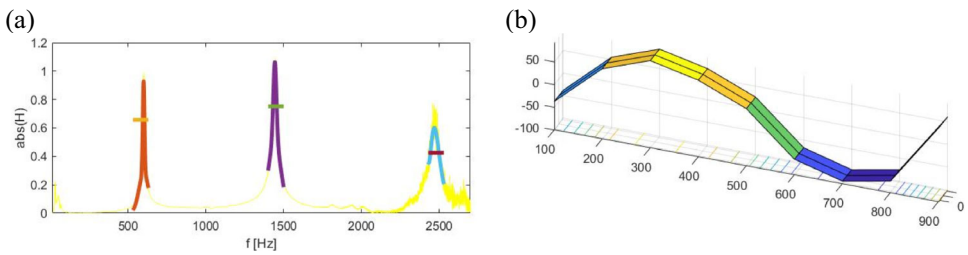

Fig. 6 **a** Absolute value of chosen frequency response function FRF, **b** the second mode shape

the subsequent measurements, around D8–D9 depending on the specimen, cracks began to appear, which became observable visually after 12–13 days (measurements D12–D13) (Fig. 9a).

While the time the specimens were immersed in the solution progressed, the cracks propagated and increased in size. A schematic representation of the cracks and how they were increased in all three specimens B1–B3 were presented in Fig. 8.

The figure shows the specimens in different views—the bottom view in the middle, both side views at the top, and the bottom and front views on the left and the right. The red line represents the precisely observed cracks obtained from the photos taken during each measurement. After measurement D8 (Fig. 8a) cracks appeared in the bottom of the specimen, which may result from the fact that the distance of the reinforced steel bar is the closest to this surface (see Fig. 2b). Then, after the following days of immersion in the solution, one main crack was observed on the bottom surface, along the steel rod, and on other surfaces as well (Fig. 8b). The last observation was conducted while measuring D76 (Fig. 8c). In addition to the main crack, many other cracks were observed on the bottom surface of the specimens and the side surfaces.

After the experimental tests were carried out, the selected specimens were cut into pieces so that the corrosion of the steel rod could be seen (Fig. 9b). As can be observed, the corrosion occurred locally, on a specific surface of the steel rod, from where the crack started to spread radially and randomly, omitting large aggregates.

4.2 Corrosion Potential Measurement

The tests conducted on samples allow us to determine the correlation between the corrosion rate, the time that specimens were immersed in the NaCl solution and the potential difference that occurred between the steel rod in concrete and the reference electrode placed in the concrete surface measured. The results obtained are presented for three specimens B1–B3 as areas where the values of the measured potential (vs $Cu|CuSO_4$) are given according to the two factors: the

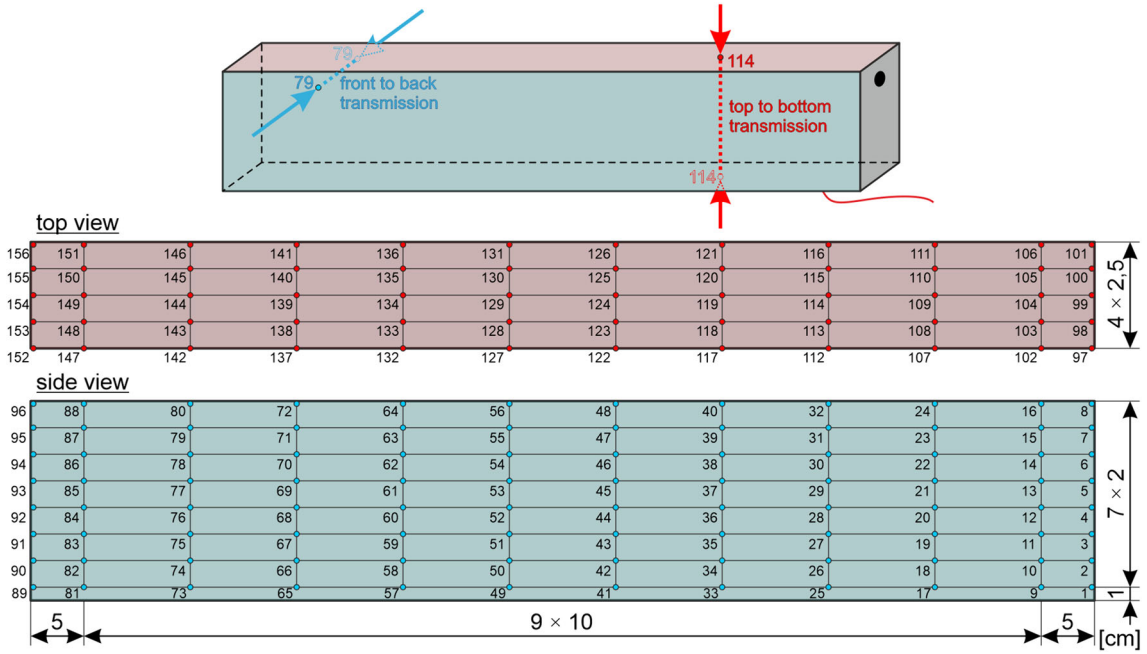

Fig. 7 Scheme of measurement points in tests with UPV

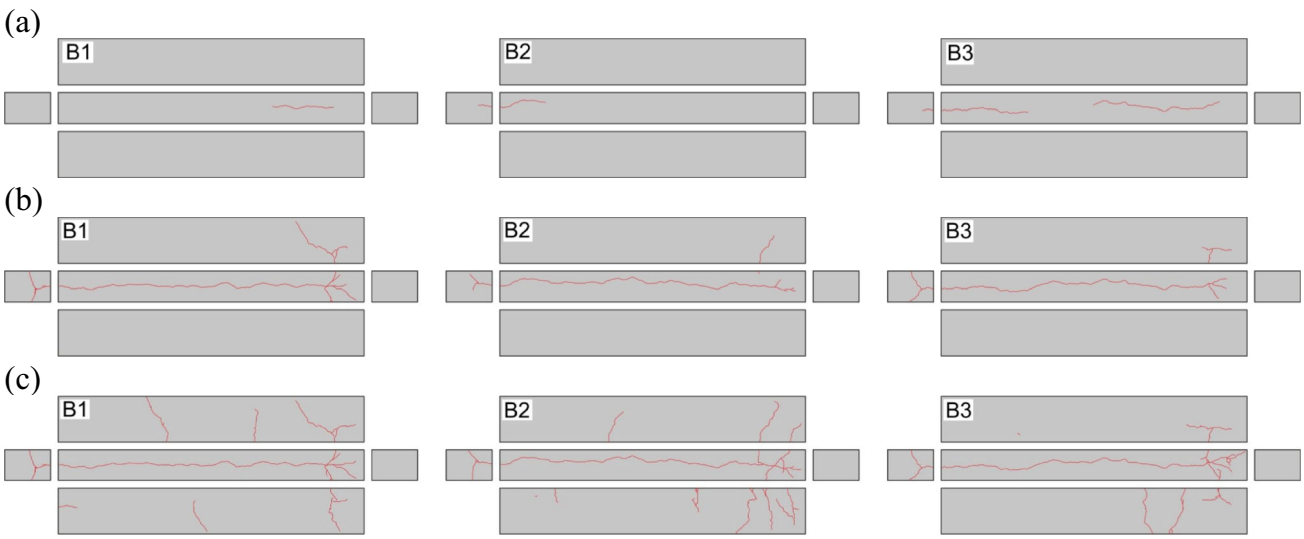

Fig. 8 Observed crack enlargement (bottom view in the middle, both side views at the top, and the bottom, and front views on the left and the right) while the time of immersion was progressing, while measurement: **a** D8, **b** D28, **c** D76

Fig. 9 The specimen during experiments **a** overall view on the bottom of the specimen after removing from the solution, **b** cross-section after experiments

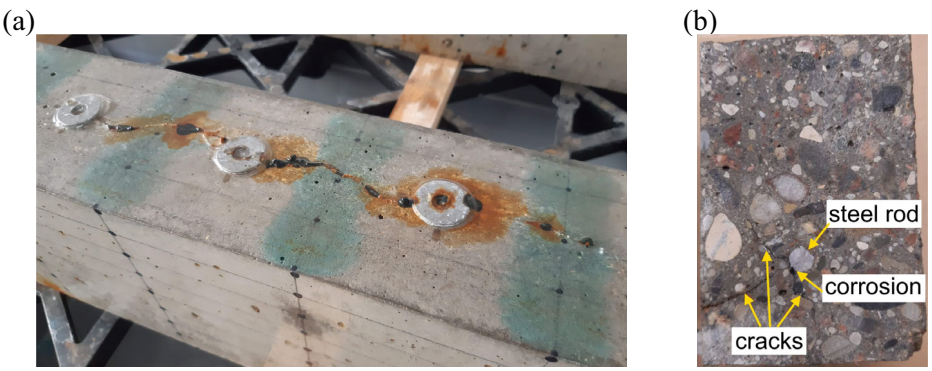

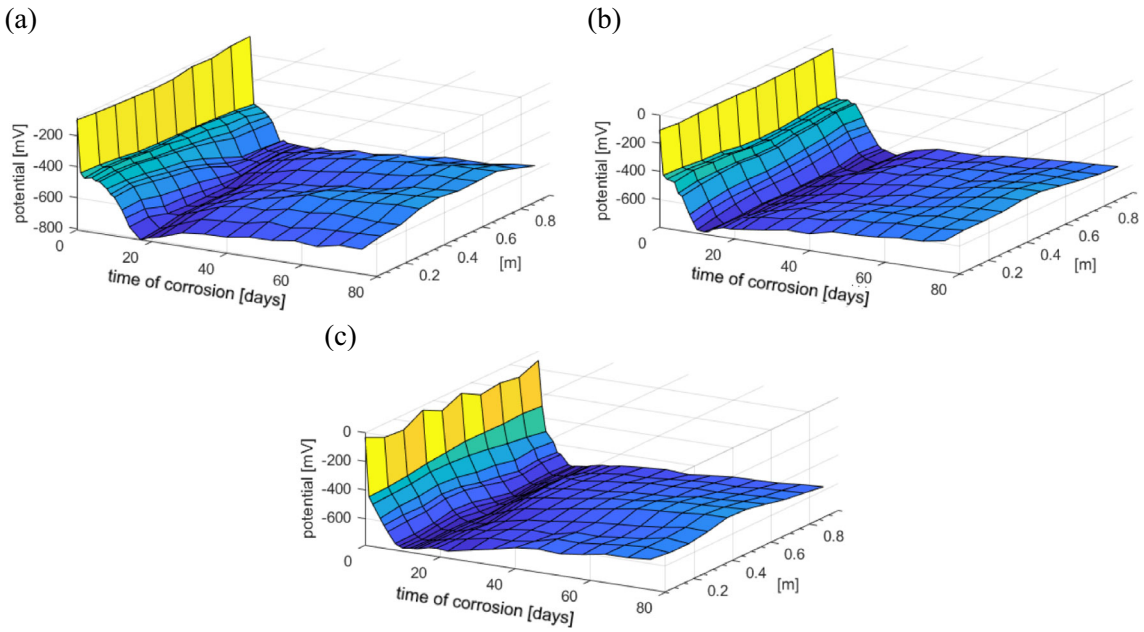

Fig. 10 Corrosion potential measurement in specimen: **a** B1, **b** B2, **c** B3

number of days that the specimens spent in the solution (see Table 1) and the location of the measuring points along the specimen length e1–e10 (Fig. 10). Location of the measuring points were constant during measurements even in the presents of cracks.

The results presented show that the value of the potential decreases at the beginning of the measurement, which is consistent with the assumption of corrosion occurrence. The average value of the measured potential after one day of keeping the specimen in the solution (measurement D1) was − 478 mV for B1, − 456 mV for B2, and − 400 mV for B3 (all vs Cu|CuSO$_4$). However, after some time, during measurements D10–D13 depending on the specimen, the value of the measured potential stopped decreasing and started to increase. The extreme value of potential was − 740 mV for B1 after measurement D13, − 770 mV for B2 after measurement D12, and − 765 mV for B3 after measurement D10 (all vs Cu|CuSO$_4$). The value of the potential then increases almost linearly. During the last measurement, D76 the values of the potential were: − 580 mV, − 579 mV, and − 580 mV (all vs Cu|CuSO$_4$) for specimens B1, B2, and B3, respectively.

4.3 Low-Frequency Vibrations

During each measurement D0–D76 natural frequencies and mode shapes for every specimen B1–B3 were determined. The values of each natural frequency were computed as a mean value obtained from each measurement. The relationships between the variation of the natural frequencies of all three samples (B1–B3) and the number of days they were immersed in the NaCl solution are presented in Fig. 11a–c, for the first, second, and third frequencies, respectively.

In measurement D0, the first determined frequencies were 540–548 Hz, the second frequencies were 1342–1360 Hz and the third were 2345–2368 Hz depending on the specimen. Then the frequencies started to increase to reach local maximum values: 589–591 Hz, 1454–1459 Hz, and 2531–2539 Hz for the first, the second, and the third natural frequencies, respectively. All values mentioned were obtained during measurement D8–D10 depending on the specimen. Then, after reaching the maximum points, the values of all three frequencies started to decrease until about measurement D19–D22. Afterward, the values started to behave differently—the first natural frequency started to increase continuously, the second frequency remained almost the same, while the third frequency decreased for some time and then remained the same. The last measured values were about 590–600 Hz, 1439–1447 Hz, and 2449–2474 Hz for the first, the second, and the third natural frequency, respectively. The example of changing the frequency values is shown in FRF graphs for measurements D0 and D10, presented in Fig. 12.

Moreover, three global mode shapes corresponding to three frequencies were determined. However, the modes were typical for freely supported beams—the first mode was half-sine shaped, and the second and the third were two- and three-half-sine shaped, respectively. The shapes remained unchanged. However, an additional peak in FFT that occurred in the FRF graphs was related to the local form of mode shape. The local mode shape occurred due to the cracking and some parts of the concrete beam were loose.

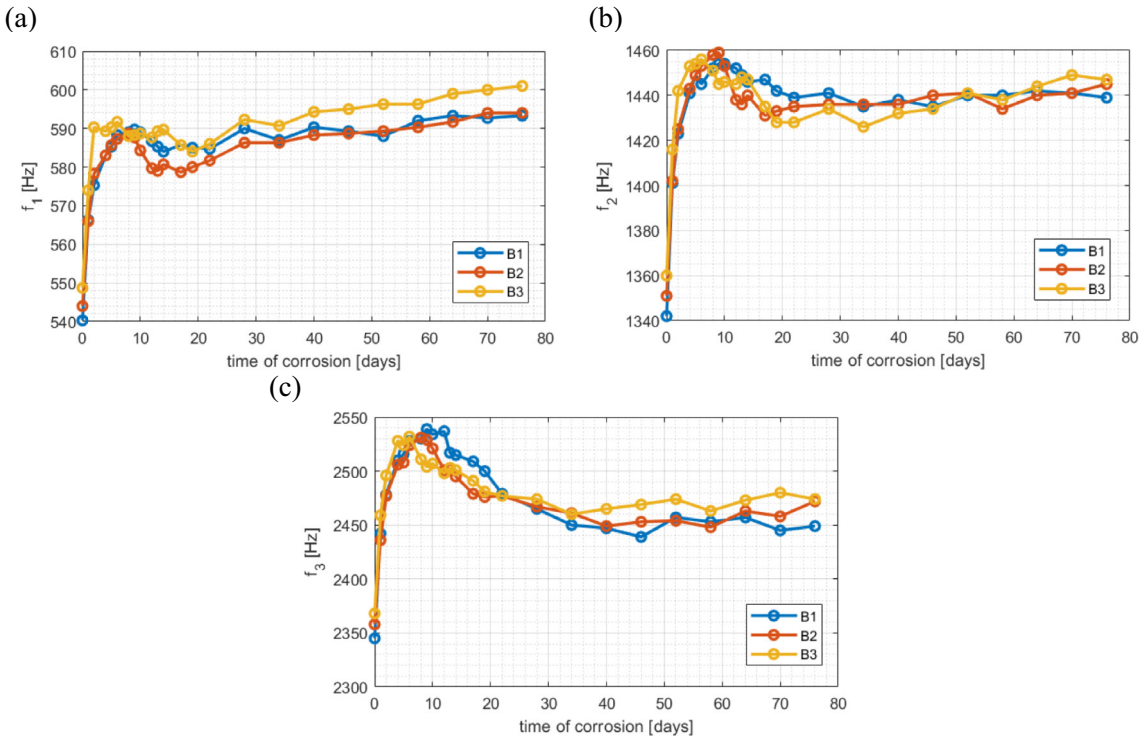

Fig. 11 Natural frequencies of specimens B1–B3: **a** the first, **b** the second, **c** the third

4.4 Ultrasonic Waves

The values of P-wave velocity were presented in Fig. 13 in the form of maps drawn individually for each beam (in columns) and chosen measurement (in rows). The values of P-wave velocity were computed as a mean value obtained from measurements repeated three times. A single velocity map is drawn for two views of the samples: top (above) and side (below). The views are separated with bold black lines. For each velocity map, a mean value, standard deviation (STD), and coefficient of variation (COV) were calculated as well. To facilitate the comparison of the P-wave velocity maps, the common color scale was used with velocity values from 2000 to 5000 m/s.

During the first phase of corrosion (measurements D0–D6) no significant variation of wave velocity was observed—low values of STD and COV (Fig. 14b). However, the mean value of wave velocity increased (Fig. 14a). This was due to the fact that during a few first measurements, the samples were soaking with water allowing the P-wave to travel with higher velocity. After 8 days of corrosion, (measurement D8) the wave velocity stopped increasing and started to decrease, and simultaneously STD and COV began to increase. This was associated with the formation of the first cracks in all beams—the maps show lower velocity values in the paths crossing the cracks. The presence of cracks led to an increase of the length of propagation paths resulting in lower values of apparent wave velocity. First, the cracks were rather shallow and present only on the upper surface thus only the upper edge on the side face of the beam was affected. As the cracks deepened, the effect was much more pronounced and could be seen in a wider range of points. This resulted in a significant decrease in the mean value of apparent velocity (this change was linearly correlated with the time of corrosion), STD and COV also increased significantly.

The vertical cracks on the side faces of the beams were not detected, because they were not perpendicular to any wave travel paths. The single horizontal crack on the side of beam B3 was not visible because it did not cross any of the wave paths. The velocity values for the vertical paths (97–156) were lower in the central part of the beam for further measurements because horizontal cracks appeared inside the beam, however, they were not visible on the surface of the beams—they ran from the bar to the sides but did not reach the side faces.

5 Discussion

5.1 Integration of Diagnostics Methods

To better characterise the corrosion process, the experimental results described in sections 4.2–4.4. were integrated and

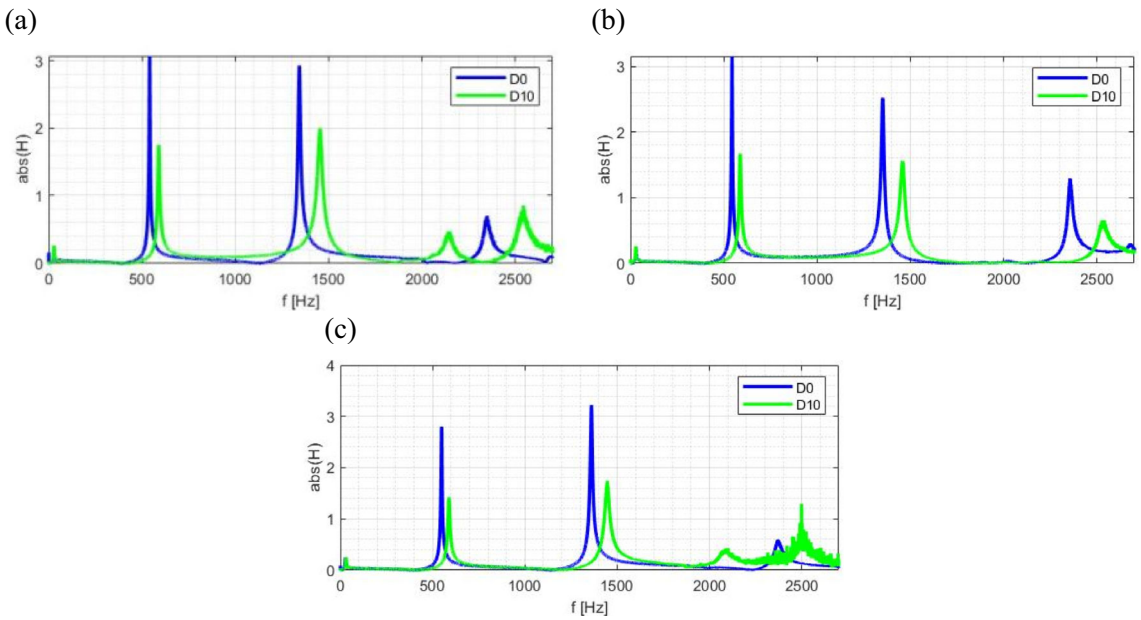

Fig. 12 FRFs for measurement D0 and D10 for beams: **a** B1, **b** B2, **c** B3

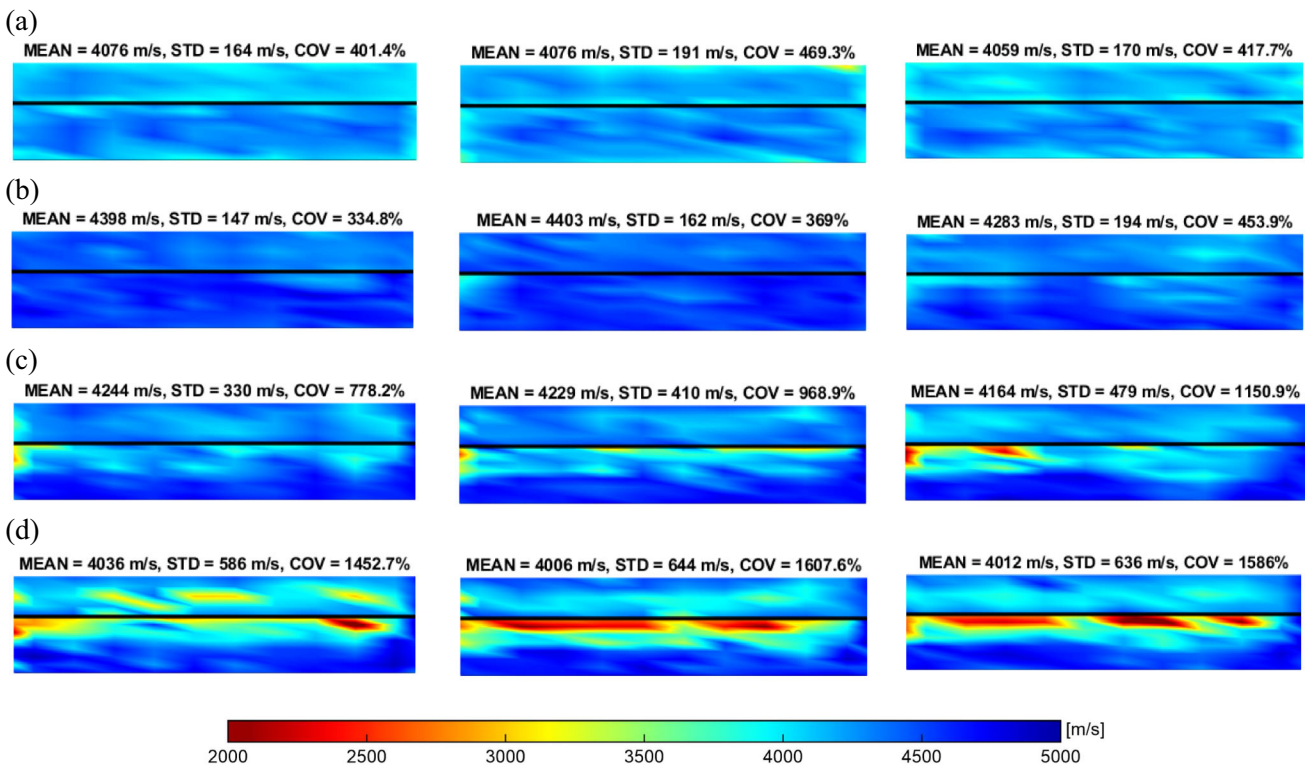

Fig. 13 P-wave velocity while time of immersion of specimens B1, B2 and B3 was progressing, while measurement: **a** D0, **b** D8, **c** D28, **d** D76. Each map contains two views: top-view (above) and side-view (below)

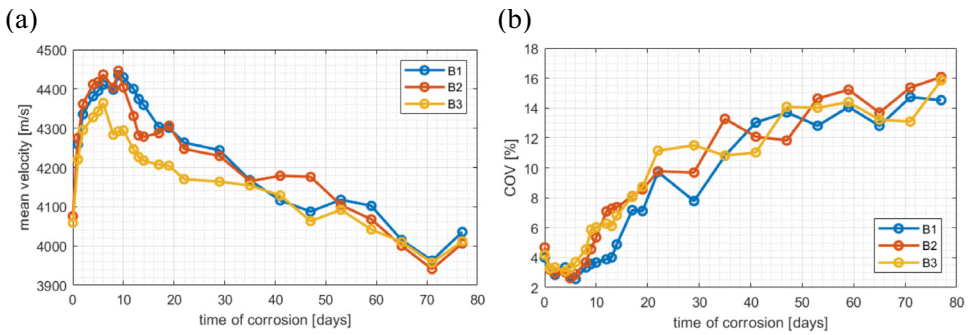

Fig. 14 The graphs: **a** mean velocity against time, **b** coefficient of variation COV against time

analysed together. Since the electrical potential technique is well studied and standardised, its results were taken as a reference and compared with other parameters (natural frequencies, mean P-wave velocity, and coefficient of variation (COV) of the P-wave velocity). Figure 15 shows the results for all beams B1–B3. To enhance the legibility of the diagrams, the potential values were averaged along the length of the beam (for all measurement points) and the vertical axis was reversed. The behaviour of all three beams was similar.

Three significant stages (stage, I, II, and III) of the cracking process were distinguished. The first stage (initiation stage), with a duration of 4 days, was related to the soaking of the concrete with water. The rapid change of electrical potential was observed between the intact state (D0) and the first day of corrosion (D1). However, further at this stage, the potential remains at a level of approximately − 500 mV for sample B1 and − 480 mV for sample B2. Sample B3 behaved differently at this stage and the potential changed gradually up to − 590 mV. According to ASTM C876-15 standard, there was a high probability of corrosion at the end of stage I. A significant increase was observed for all three eigenfrequencies (Fig. 15a), probably caused by soaking with water. A major growth was also observed in the P-wave velocity (Fig. 15b), as already mentioned in the previous section. It is important to note that the COV had low values, not exceeding 1.1%, and initially decreased as water absorption led to more uniform mass distribution, and consequently, the P-wave velocity varied less throughout the sample.

The second stage—known as the propagation stage, lasting approximately between 4 and 14 days of immersion in the solution, was associated with a gradual increase in the level of corrosion, which could be observed by the significant change in the electrical potential. Peak potential values were observed at this stage. In the case of natural frequencies (Fig. 15a), their values also reached peaks and began to decrease, indicating the important influence of corrosion on the dynamic behaviour in the low-frequency range (as mentioned in the previous section, the first surface cracks appeared). Similar observations could be made based on the P-wave velocity changes (Fig. 15b), which also reached peaks and decreased. This indicated the end of water absorption, which revealed the influence of corrosion on high-frequency wave propagation. The COV also began to change significantly (Fig. 15c), reaching approximately 1.2–1.5% at the end of stage II.

The third stage (after 14 days until the end of the tests) was related to the severe mechanical degradation of the samples due to the appearance of cracks caused by the increase in the volume of the corroded rod. It is important to note that at stage III electrical potential appeared to be relatively insensitive to the level of damage, considering how advanced the fracture of samples was. Only a small change in potential was observed for all beams (final values were around –590 mV). In the case of the natural frequencies (Fig. 15a), their differences could be clearly distinguished. After a slight decrease in all three eigenfrequencies, the first one increased slightly, whereas the second and the third remained at approximately the same level. Similarly to the electrical potential, the natural frequencies were rather insensitive to the level of damage. Significantly different observations could be made for the mean P-wave velocity values (Fig. 15b), which decreased rapidly at this stage due to the elongation of the propagation path in the crack area near the corroded rod (cf. Figure 13). For the same reason a rapid increase in COV was observed (Fig. 15c), eventually exceeding 3.5%.

5.2 Diagnostic Framework

To sum up all the remarks made in the previous subsection it can be stated that the measurement of electrical potential is very efficient in the detection of corrosion process at its initial state (stages I and II). However, it appears to be less useful for quantitative assessment of the level of corrosion as it progresses. Similar conclusions were reached for natural frequencies. To characterise the severity of damage P-wave velocity measurements are more promising. Based on the analysis carried out, an attempt has been made to develop a two-stage diagnostic framework for the characterisation of corrosion-induced concrete fracture. The proposed scheme can be applied to reinforced concrete beams similar to those considered in the study.

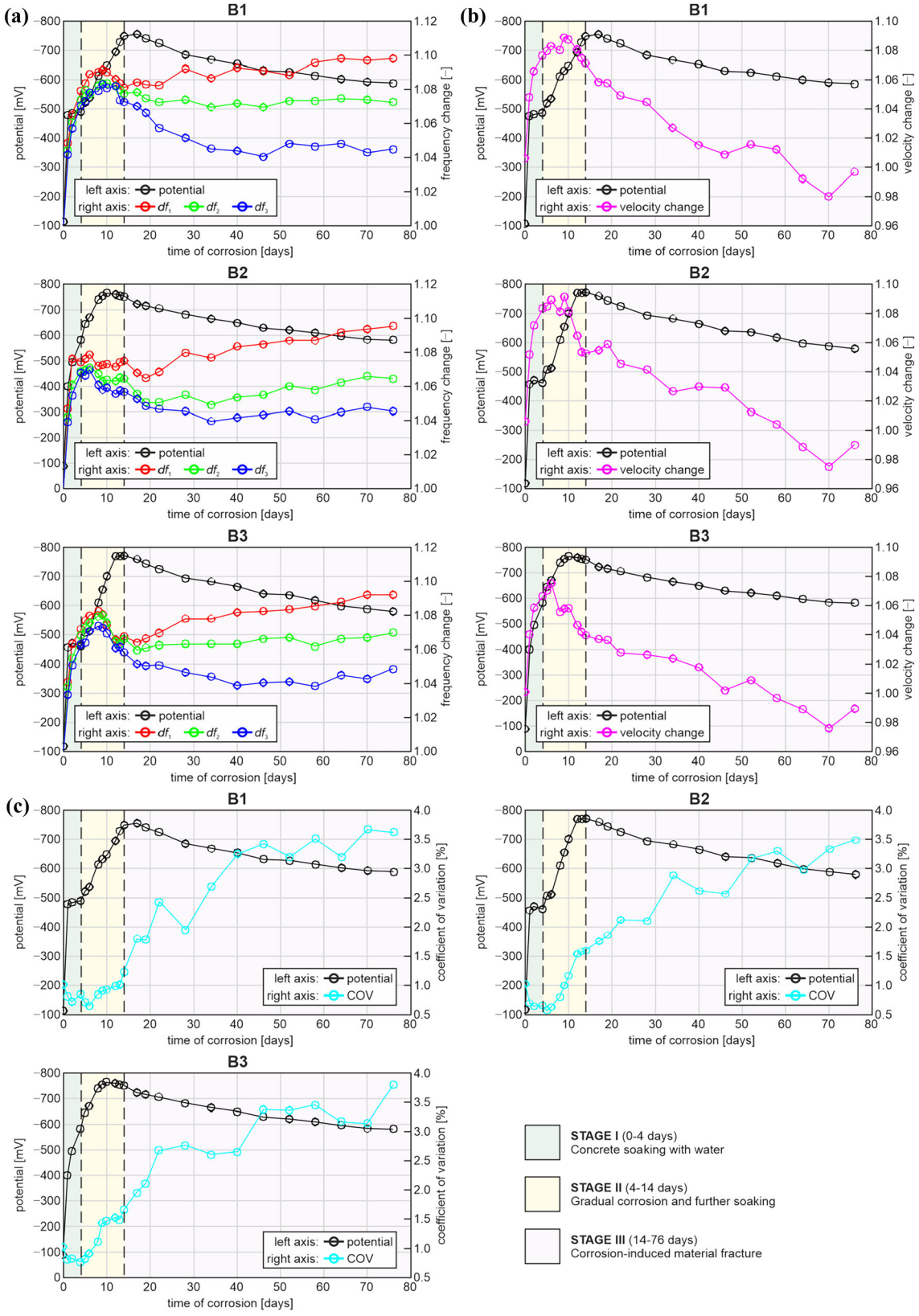

Fig. 15 Comparison of electrical potential with other diagnostic parameters (for all beams B1–B3): **a** change of natural frequencies, **b** change of P-wave velocity, **c** coefficient of variation of P-wave velocity

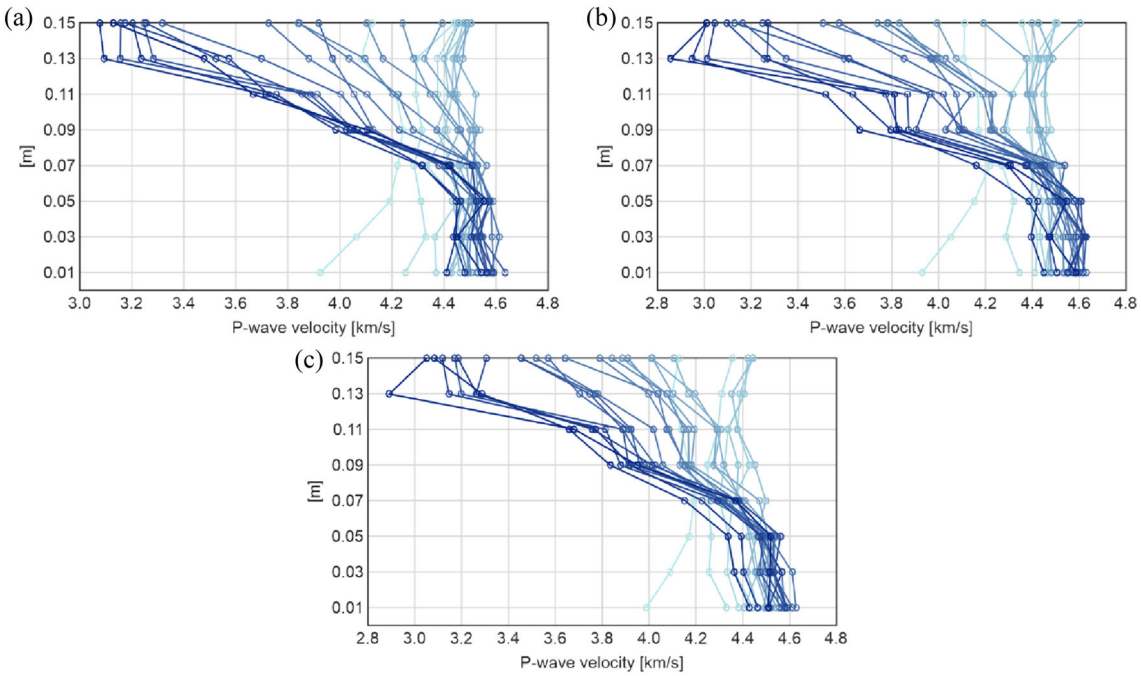

Fig. 16 P-wave velocity along the height of each beam (propagation from side to side of the beam; the longer corrosion the darker the curve): **a** B1, **b** B2, **c** B3

The first step in the corrosion detection process is the measurement of the electrical potential (step A). The number of measuring points can be reduced to 10 points along a single line in the axis of the beam, according to small changes in the electrical potential across the surface of the beam. The monitoring of changes in the electrical potential can be continued until the potential values reach a peak. It can be expected that further measurements would not provide any more important information. At this moment, P-wave velocity measurements can be considered efficient (stage B). Based on the increasing time of flight of the wave, the severity of damage can be assessed. It is important to note that the P-wave velocity changes over the height of the beam, from the top (where there is a corroded bar) to the bottom (where there is no reinforcement) are significant. The mean P-wave velocity at each horizontal line at the side surface of each beam is presented in Fig. 16 for all measurements (the longer the corrosion, the darker the curve).

It is visible that the velocity does not change significantly at the bottom of the beam (except for the initial increase due to water absorption). Higher variations are observed at the top line, where a longitudinal crack appears in the vicinity of the reinforcing bar. More importantly, the difference between the P-wave velocities at the top and bottom of the beam increases with the duration of corrosion time. This can also be seen in the P-wave velocity maps in Fig. 13.

Since the P-wave velocity measurements are time-consuming, it is suggested to reduce the number of measurement points to two lines on the side of the beam, one at the top (near reinforcement) and one at the bottom (far from reinforcement) edges (points 1, 9, …, 81, 89 and 8, 16, …, 88, 96, cf. Figure 7). The difference between the mean P-wave velocity values at the top and bottom lines can indicate the developing crack. To verify this recommendation, the ratio of P-wave velocities at the top and bottom lines was calculated (Fig. 17).

It is visible that in the early stages of corrosion, the difference is insignificant and does not exceed 5%. This level of change may not be an indication of damage, it may just be the effect of concrete being a heterogeneous material. However, small internal cracks may occur in this stage. If the velocity difference exceeds 5% (ratio below 0.95), it can be considered as the beginning of fracture. This threshold is associated with the appearance of the first surface cracks in beams (B1—measurement D8, B2–D10, and B3–D13). Based on these observations, a ratio of the P-wave velocity at the top and bottom lines of the beam ($C_{L,t}$ and $C_{L,b}$, respectively) can be considered as a damage index with:

$$DI = \frac{C_{L,t}}{C_{L,b}} \leq 0.95 \tag{2}$$

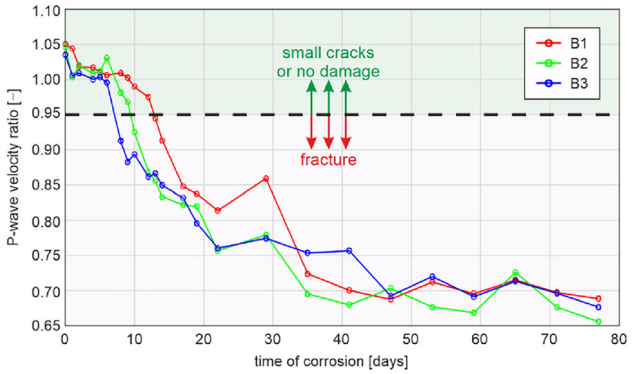

Fig. 17 The ratio of P-wave velocity at the top and bottom line on the side of each beam

6 Conclusions

The paper deals with non-destructive diagnostics of reinforced concrete beams subjected to accelerated electrochemical corrosion. Three specimens (B1-B3) were examined using the potential measurement method, low-frequency vibrations, and ultrasonic wave propagation to study the corrosion-induced mechanical degradation of RC samples. The corrosion was successfully induced and progressed for a total time of 76 days with 24 breaks during which measurements with all methods were conducted.

Based on the variety of measured factors, three stages of corrosion were distinguished. During the first stage, the onset of corrosion was indicated by the rapid increase in electrical potential. The natural frequencies and the mean values of the P-wave velocity also increased rapidly, however, this could be an effect of water absorption. In the second stage, the corrosion process developed and led to the appearance of cracks. The electrical potential, all the eigenfrequencies, and the mean P-wave velocity reached extreme values and then started to decrease. During the third stage, serious mechanical degradation was observed due to crack development. The severity of the damage could be described by the mean P-wave velocity as all other factors did not change significantly.

A diagnostic framework has been proposed to characterise corrosion-induced fracture in reinforced concrete. Considering the capabilities and limitations of the methods applied, it was concluded that at the first two stages of corrosion (I and II), it is efficient to use the electrical potential method to detect and measure the level of corrosion. However, at the third stage (III), when the fracture process initiates, it is relevant to use the P-wave velocity to measure the severity of mechanical degradation by a proposed damage index that reflects the differences in P-wave velocity in the area of the reinforcement and away from its vicinity.

The occurrence of corrosion in reinforced concrete structures is usually visually detected by the presence of surface cracking. However, this mainly applies to the serious damage leading to catastrophic failure. The diagnostic framework developed in this paper is capable of successfully detecting, quantitatively measuring, and monitoring the corrosion process and its consequences at its early stages using non-destructive techniques.

Acknowledgements Financial support of these studies from Gdańsk University of Technology by the DEC-49/2020/IDUB/I.3.3 grant under the ARGENTUM TRIGGERING RESEARCH GRANTS - 'Excellence Initiative - Research University' program is gratefully acknowledged.

Author Contributions Conceptualization: TF, EW, BM, MR; methodology: TF, EW, BM, JR, MR; writing—original draft preparation: TF; writing—review and editing: TF, EW, BM, JR, KW, MR; visualization: TF, EW;supervision: KW, MR; project administration: TF; All authors have read and agreed to the published version of the manuscript.

Funding Financial support of these studies from Gdańsk University of Technology by the DEC-49/2020/IDUB/I.3.3 grant under the ARGENTUM TRIGGERING RESEARCH GRANTS—'Excellence Initiative—Research University' program is gratefully acknowledged.

Data Availability and Materials The datasets generated and analyzed during conducted experiments are included in this published article. The raw data are available from the corresponding author on reasonable request.

Declarations

Competing interests The authors declare that they have no competing interests as defined by Springer, or other interests that might be perceived to influence the results and/or discussion reported in this paper.

Ethical Approval Not applicable.

References

1. Mehta, P.K., Monteiro, P.J.: Microstructure and properties of hardened concrete. Concrete: Microstructure, properties, and materials, pp.41–80 (2006)
2. Cui, X., Wang, Q., Li, S., Dai, J., Xie, C., Duan, Y., Wang, J.: Deep learning for intelligent identification of concrete wind-erosion damage. Autom. Constr. **141**, 104427 (2022). https://doi.org/10.1016/j.autcon.2022.104427
3. Zheng, Z., Su, C., Pan, X., Sun, Y., Yuan, W., Wang, W.: Quantitative damage evaluation of prestressed concrete containments with

steel fiber strengthening under internal pressure. Eng. Struct. **278**, 115494 (2023). https://doi.org/10.1016/j.engstruct.2022.115494
4. Fu, C., Jin, N., Ye, H., Jin, X., Dai, W.: Corrosion characteristics of a 4-year naturally corroded reinforced concrete beam with load-induced transverse cracks. Corros. Sci. **117**, 11–23 (2017). https://doi.org/10.1016/j.corsci.2017.01.002
5. Rodrigues, R., Gaboreau, S., Gance, J., Ignatiadis, I., Betelu, S.: Reinforced concrete structures: A review of corrosion mechanisms and advances in electrical methods for corrosion monitoring. Constr. Build. Mater. **269**, 121240 (2021). https://doi.org/10.1016/j.conbuildmat.2020.121240
6. Zhu, X., Zi, G.: A 2D mechano-chemical model for the simulation of reinforcement corrosion and concrete damage. Constr. Build. Mater. **137**, 330–344 (2017). https://doi.org/10.1016/j.conbuildmat.2017.01.103
7. El Alami, E., Fekak, F.E., Garibaldi, L., Elkhalfi, A.: A numerical study of pitting corrosion in reinforced concrete structures. J. Build. Eng. **43**, 102789 (2021). https://doi.org/10.1016/j.jobe.2021.102789
8. Krykowski, T., Jaśniok, T., Recha, F., Karolak, M.: A cracking model for reinforced concrete cover, taking account of the accumulation of corrosion products in the ITZ layer, and including computational and experimental verification. Materials **13**(23), 5375 (2020)
9. Abbas, H., Elsanadedy, H., Alaoud, L., Almusallam, T., Al-Salloum, Y.: Effect of confining stirrups and bar gap in improving bond behavior of glass fiber reinforced polymer (GFRP) bar lap splices in RC beams. Constr. Build. Mater. **365**, 129943 (2023)
10. Jaśniok, M., Jaśniok, T.: Corrosion diagnostics performed on cores drilled from concrete structures, using the laboratory simulation of temperature and relative humidity impact. Appl. Sci. **12**, 7134 (2022). https://doi.org/10.3390/app12147134
11. Jin, X., Tong, J., Tian, Y., Jin, N.: Time-varying relative displacement field on the surface of concrete cover caused by reinforcement corrosion based on DIC measurement. Constr. Build. Mater. **159**, 695–703 (2018)
12. Al-Akhras, N., Aleghnimat, R.: Evaluating corrosion deterioration in self-compacted reinforced concrete beams and prisms using different tests. Constr. Build. Mater. **256**, 119347 (2020). https://doi.org/10.1016/j.conbuildmat.2020.119347
13. Maalej, M., Chhoa, C.Y., Quek, S.T.: Effect of cracking, corrosion and repair on the frequency response of RC beams. Constr. Build. Mater. **24**, 719–731 (2010). https://doi.org/10.1016/j.conbuildmat.2009.10.036
14. Lejouad, C., Richard, B., Mongabure, P., Capdevielle, S., Ragueneau, F., et al.: Effect of steel reinforcement corrosion on the dynamic behavior of RC beams. FONTEVRAUD9—International Symposium: Contribution of Materials Investigations and Operating Experience to Light Water NPPs' Safety, Performance and Reliability, Sep2018, Avignon, France. cea-02338541
15. Zhang, L., Sun, L., Dong, L.: Experimental study on the relationship between the natural frequency and the corrosion in reinforced concrete beams. Adv. Mater. Sci. Eng. **2021**, 1–10 (2021). https://doi.org/10.1155/2021/9976738
16. Ervin, B.L., Kuchma, D.A., Bernhard, J.T., Reis, H.: Monitoring corrosion of rebar embedded in mortar using high-frequency guided ultrasonic waves. J. Eng. Mech. **135**(1), 9–19 (2009)
17. Sharma, A., Sharma, S., Sharma, S., Mukherjee, A.: Ultrasonic guided waves for monitoring corrosion of FRP wrapped concrete structures. Constr. Build. Mater. **15**(96), 690–702 (2015). https://doi.org/10.1016/j.conbuildmat.2015.08.084
18. Choi, H., Bittner, J., Popovics, J.S.: Comparison of ultrasonic imaging techniques for full-scale reinforced concrete. transportation research record. J. Transport. Res. Board **2592**, 126–135 (2016). https://doi.org/10.3141/2592-14
19. Ghosh, D., Kumar, R., Ganguli, A., Mukherjee, A.: Non-destructive evaluation of rebar corrosion-induced damage in concrete through ultrasonic imaging. J. Mater. Civ. Eng. **32**(10), 04020294 (2020). https://doi.org/10.1061/(ASCE)MT.1943-5533.0003398
20. Mayakuntla, P.K., Ganguli, A., Smyl, D.: Gaussian mixture model-based classification of corrosion severity in concrete structures using ultrasonic imaging. J. Nondestr. Eval. **42**(2), 28 (2023). https://doi.org/10.1007/s10921-023-00939-9
21. Mayakuntla, P.K., Ghosh, D., Ganuli, A.: Nondestructive evaluation of rebar corrosion in concrete structures using ultrasonics and laser-based sensing. Nondestruct. Test. Eval. **37**(3), 297–314 (2022). https://doi.org/10.1080/10589759.2021.1998489
22. Niederleithinger, E., Wolf, J., Mielentz, F., Wiggenhauser, H., Pirskawetz, S.: Embedded ultrasonic transducers for active and passive concrete monitoring. Sensors **15**(5), 9756–9772 (2015). https://doi.org/10.3390/s150509756
23. Goyal, P., Sharma, S., Kwatra, N.: Acoustic emission monitoring of steel fiber reinforced beams under simultaneous corrosion and sustained loading. Eur. J. Environ. Civ. Eng. (2022). https://doi.org/10.1080/19648189.2022.2087743
24. Goldaran, R., Turer, A., Kouhdaragh, M., Ozlutas, K.: Identification of corrosion in a prestressed concrete pipe utilizing acoustic emission technique. Constr. Build. Mater. **242**, 118053 (2020). https://doi.org/10.1016/j.conbuildmat.2020.118053
25. Yanjie, B., Hui, S., Bai, Y., Cai, Y.: Mechanical properties and damage mechanisms of concrete under four temperature gradients combined with acoustic emission method. J Build Eng **57**, 104906 (2022). https://doi.org/10.1016/j.jobe.2022.104906
26. Han, J., Miao, Z., Wang, J., Zhang, X., Lv, Y.: Investigation of the corrosion-induced damage mechanism of steel fibers in ultra-high-performance steel fiber-reinforced concrete using X-ray computed tomography. Constr. Build. Mater. **368**, 130429 (2023). https://doi.org/10.1016/j.conbuildmat.2023.130429
27. Fabien Bernachy-Barbe, T.S., Dewynter-Marty, V., L'Hostis, V.: Using X-ray microtomography to study the initiation of chloride-induced reinforcement corrosion in cracked concrete. Constr. Build. Mater. **259**, 119574 (2020). https://doi.org/10.1016/j.conbuildmat.2020.119574
28. Samanta, R., Alessandro, T., Jelke, D., Ignasi, F., Karin, L.: A closer look at corrosion of steel reinforcement bars in concrete using 3D neutron and X-ray computed tomography. Cement and Concrete Research, Vol. 144, p. 106439 (2021) https://doi.org/10.1016/j.cemconres.2021.106439
29. Gaon, J., Jin, Wu., Li, J., Zhao, X.: Monitoring of corrosion in reinforced concrete structure using Bragg grating sensing. NDT&E International **44**, 202–205 (2011). https://doi.org/10.1016/j.ndteint.2010.11.011
30. Wonga, P.T.W., Lai, W.W.L., Sham, J.F.C., Poon, C.-S.: Hybrid non-destructive evaluation methods for characterizing chloride-induced corrosion in concrete. NDT and E Int. **107**, 102123 (2019). https://doi.org/10.1016/j.ndteint.2019.05.008
31. Chen, J., Chuanqing, Fu., Ye, H.: Xianyu Jin (2020) Corrosion of steel embedded in mortar and concrete under different electrolytic accelerated corrosion methods. Constr. Build. Mater. **241**, 117971 (2020). https://doi.org/10.1016/j.conbuildmat.2019.117971
32. Dai, M., Yang, O., Xiao, Y., et al.: Influence of longitudinal bar corrosion on impact behavior of RC beams. Mater. Struct. **49**, 3579–3589 (2016). https://doi.org/10.1617/s11527-015-0741-0
33. Tondolo, F.: Bond behaviour with reinforcement corrosion. Constr. Build. Mater. (2015). https://doi.org/10.1016/j.conbuildmat.2015.05.067